Simulation of particle velocity in a laser-produced tin plasma extreme ultraviolet source

Majid Masnavi,[1,a)] Mitsuo Nakajima,[1] Kazuhiko Horioka,[1] Homaira Parchamy Araghy,[2] and Akira Endo[3]
[1]*Department of Energy Sciences, Tokyo Institute of Technology, 4259 Nagatsuta, Midori-ku, Yokohama 226-8502, Japan*
[2]*Plasma Physics Research Center, Azad University, Tehran, Iran*
[3]*Friedrich-Schiller University, Institute of Applied Physics, Jena, Germany*

(Received 3 March 2011; accepted 14 May 2011; published online 29 June 2011)

In connection with fast heating in a laser produced plasma (LPP) extreme ultraviolet (EUV) source, the superheating behavior of bulk tin (Sn) at high heating rates is investigated. A constant temperature and pressure molecular dynamics simulation using modified Lennard-Jones and Coulomb potentials suitable for studying the liquid structure of Sn is employed in order to derive the caloric curves of the solid and liquid phases. The results have shown transient effects on the phase transitions. Superheating is observed during the melting and vaporizing processes. The velocity distribution of Sn particles against typical laser fluence in a LPP EUV light source has been numerically investigated using a simplified method including a one-dimensional, two-temperature, molecular dynamics, and steady-state ionization model. In the framework of our model, it was found that ejected Sn particles have a maximum velocity on the order of 10 to 40 km/s in plasma created using a nanosecond pre-pulse neodymium-doped yttrium aluminum garnet (Nd:YAG, 1.06 μm) laser in EUV lithography experiments. © *2011 American Institute of Physics*. [doi:10.1063/1.3601346]

I. INTRODUCTION

Recent advances in the field of extreme ultraviolet (EUV) lithography have revealed that laser-produced or discharge-produced lithium and tin plasmas[1–5] are source candidates for next-generation microelectronics. Tin (Sn) material demonstrated a large conversion efficiency of input power to emission in a 2% bandwidth centered on the wavelength $\lambda = 13.5$ nm, the so-called in-band radiation.[6–8] The large conversion efficiency (CE) is formed in the low ion density region of 10^{17}–10^{18} cm^{-3} due to the opacity effect. It has been demonstrated that a high CE and a lower debris laser-based EUV source can be realized by using a mass-limited Sn target and a double laser pulse irradiation scheme. The use of pre-pulse irradiation is indispensable for improving the density distribution via the expansion of Sn particles before firing a carbon dioxide (CO2) laser (10.6 μm) as a main pumping source. Typically a sub-nanosecond (ns) neodymium-doped yttrium aluminum garnet (Nd:YAG, 1.06 μm) laser having an intensity of 10^9 to 10^{12} W cm^{-2} produces the pre-pulse radiation.[9–13] Though there are many experimental results on the double laser pulse irradiation scheme, however, calculation efforts to estimate the thermodynamical behavior of Sn with such high heating rates and velocity distributions in conditions relevant to laser-based EUV sources have not been reported.

In this article, in order to investigate the thermodynamical behavior and velocity distribution of Sn particles, a simplified method including a one-dimensional two-temperature model coupled to molecular dynamics and steady-state ionization is used. A computational method and assumptions are described briefly in Sec. II. The calculation results are presented and discussed in Sec. III, for conditions relevant to laser produced plasma EUV sources. This is followed by the conclusions.

II. CALCULATION METHOD AND ASSUMPTIONS

In metals, the absorption of laser light takes place via the conduction band electrons. Once the electrons are heated up, the energy is transferred to the lattice via electron-phonon coupling. In the framework of a one-dimensional two-temperature model (TTM), the temporal and spatial evolution of the lattice and electron temperatures, T_l and T_e, are described by two coupled nonlinear differential equations as

$$C_e(T_e)\,\partial_t T_e = \nabla[K_e(T_e,T_l)\nabla T_e] - G(T_e - T_l) + S(z,t), \tag{1}$$

$$C_l(T_l)\,\partial_t T_l = \nabla[K_l(T_l)\nabla T_l] + G(T_e - T_l), \tag{2}$$

where C and K are the heat capacity and thermal conductivity of the electron and lattice as denoted by the subscripts e and l, and G is the electron-phonon coupling constant. The source term $S(z,t)$ in the z direction, with z being the direction normal to the sample surface, is used to describe the local laser energy deposition per unit area and unit time during the laser pulse duration.

The electron heat capacity can be obtained by

$$C_e(T_e) = \gamma T_e (T_e < T_F) = 3N_e k_B/2 (T_e \geq T_F), \tag{3}$$

where $\gamma = \pi^2 N_e k_B/2T_F \simeq 56$ J m^{-3}K^{-2} is a material constant, $T_F \simeq 51272$ K is the Fermi temperature, $N_e \simeq 4.22 \times 10^{28}$ m^{-3}

a)Author to whom correspondence should be addressed. Electronic mail: masnavimajid@yahoo.com.

is the density of free electrons, and k_B is Boltzmann's constant. The electron thermal conductivity is modeled by[14]

$$K_e(T_e,T_l)=A\theta_e\frac{(\theta_e^2+0.16)^{5/4}(\theta_e^2+0.44)}{(\theta_e^2+0.092)^{1/2}(\theta_e^2+B\theta_l)}, \quad (4)$$

where $\theta_e=T_e/T_F$ and $\theta_l=T_l/T_F$. $A\simeq 66.8$ $\mathrm{Wm^{-1}K^{-1}}$ and $B\simeq 0.16$ are material constants. Equation (4) is believed to be valid in a wide range of temperatures.

The temperature dependence of the volumetric lattice heat capacity is described using[15] $C_l=2.5\times10^5$ (9.97 - 9.15 $\times 10^{-3}$ $T_l+6.5\times10^{-6}T_l^2$) $\mathrm{Jm^{-3}K^{-1}}$. Because the expressions for K_l and G weakly depend on the temperature,[16,17] we have assumed that $K_l=67$ $\mathrm{Wm^{-1}K^{-1}}$ and $G=\pi^4(N_e C_s k_B)^2/18K_e\simeq 2.04\times10^{17}$ $\mathrm{Wm^{-3}K^{-1}}$. Here, the values of the speed of sound $C_s\simeq 2730$ m/s and K_e are assumed at room temperature.

The simplest form of the laser source term S, at time t and position z, is given by

$$S(z,t)=I(t)(1-R)\alpha e^{-\alpha z}, \quad (5)$$

where $R\simeq 0.7$ (Ref. 18) and $\alpha\simeq 2\times10^7\mathrm{m^{-1}}$ (Ref. 19) are, respectively, the reflection and an absorption coefficient of the Sn target at a wavelength of 1.06 μm. The intensity $I(t)$ is assumed to have a nearly Gaussian profile with time t in the laboratory frame, so it can be described as

$$I(t)=\beta I_0 e^{-(t-\tau)^2/2\sigma^2}. \quad (6)$$

Here, β, which is assumed to be $\simeq$1, is the shielding coefficient at the target that depends on the plume temperature and species (neutrals, ions, and electrons) above the target, and 2σ, τ, and I_0 are the full width at half maximum (FWHM), time of peak intensity, and peak intensity of the laser beam, respectively.

The heat source term as the boundary condition at the target surface is expressed as

$$K_e\partial_z T_e=-(1-R)I(t), \quad z=0. \quad (7)$$

The TTM is solved by a finite difference method.

In order to investigate the particle dynamics, we have used the classical molecular dynamics (MD) method.[20] The interaction between the particles of the system was governed by a modified Lennard-Jones (MLJ) potential U_{MLJ},[21] and the particular parameters for Sn were taken from Ref. 22, with the Coulomb potential U_{C} defined as

$$U(r_{ij})=U_{\mathrm{MLJ}}+U_{\mathrm{C}}=4\epsilon\left[\left(\frac{\sigma}{r_{ij}}\right)^{12}-\left(\frac{\sigma}{r_{ij}}\right)^{6-\theta}\right]+\frac{1}{4\pi\epsilon_0}\frac{q_iq_j}{r_{ij}}, \quad (8)$$

where $\epsilon\simeq 0.0619$ eV is the depth of the potential well, $\theta\simeq 1.29$, $\sigma\simeq 0.3$ nm, r_{ij} is the magnitude of the distance between the centers of particles i and j, q is the electric charge of the particle, and ϵ_0 is the permittivity of free space. The MLJ potential is derived using an experimental radial distribution function, a dense gas-like model, the Born–Green formula, and experimental viscosity data for liquid Sn.

A detailed description of the MD model can be found elsewhere.[20,21,23–26] Briefly, at each time step [$\delta t=1$ femtosecond (fs)], the total force, velocity, position, and electric charge of all of the particles are calculated. The force vector acting on particle i from particle j is

$$\vec{F_{ji}}=F(r_{ji})\vec{r_{ji}^0}=-\frac{\partial U(r_{ji})}{\partial r}\vec{r_{ji}^0}=\frac{q_iq_j}{4\pi\epsilon_0}\frac{\vec{r_{ji}^0}}{r_{ji}^2}+\frac{24\epsilon}{r_{ji}}\left[2\left(\frac{\sigma}{r_{ji}}\right)^{12}-\frac{(6-\theta)}{6}\left(\frac{\sigma}{r_{ji}}\right)^{6-\theta}\right]\vec{r_{ji}^0}, \quad (9)$$

where $\vec{r_{ji}^0}$ is the unit vector of $\vec{r}_{ji}$, the position vector from j to i. The total force on particle i is the summation of the force vectors from all neighboring particles. The macroscopic parameters such as temperature and pressure that include a virial coefficient were evaluated at each time step. The long-range contribution to the potential energy and pressure of the entire system is explicitly included.

Calculations are initiated with particles occupying ideal crystalline lattice positions in the x, y, and z directions and random velocities from a Maxwell–Boltzmann distribution. In the present article, the periodic boundary condition is used to simulate the thermodynamical behaviors of bulk Sn. In order to obtain a relatively simple scenario that is applicable to the onset of a phase transition, we probe the dynamics of Sn particles in a series of constant pressures and temperatures, namely, an NPT ensemble with a constant particle number (N), constant external pressure (P), and constant temperature (T). The temperature and pressure were kept constant using the Berendsen method,[20,25,27] and the equations of motion were integrated using the fourth order Gear's predictor-corrector method.

In order to investigate the particle velocity in a laser produced plasma (LPP) EUV source, an open boundary condition is used. The temporal and spatial electron and lattice temperatures under given laser conditions are calculated using a TTM. Using the electron temperature and steady-state ionization model, the electric charges of all of the particles are calculated.[8] The lattice temperature is updated by scaling the velocities of all particles by a factor $\chi=\sqrt{1+G(T_e-T_l)\delta t/E_{k,t}}$ at each time step.[28–30] Here, $E_{k,t}$ is the kinetic energy at the time t at which the bulk velocity is excluded in the velocity scaling as

$$E_k=\frac{1}{2}m\sum_{i=1}^{N}\left(v_{i,1}-\bar{v}_1\right)^2+\left(v_{i,2}-\bar{v}_2\right)^2+\left(v_{i,3}-\bar{v}_3\right)^2, \quad (10)$$

where m is the mass of the Sn atom and $v_{i,j}$ and $\bar{v}_j$ ($j=1,2,3$) are the velocity of atom i and the average velocity in the x, y, and z directions for atoms in a layer normal to the laser beam. The new velocity $v'_{i,j}$ of atom i is calculated as

$$v'_{i,j}=\left(v_{i,j}-\bar{v}_j\right)\times\chi+\bar{v}_j, \quad j=1,2,3. \quad (11)$$

III. RESULTS AND DISCUSSION

Starting with a Sn film at a uniform temperature, Fig. 1(a) shows the time-dependence of the electron and lattice

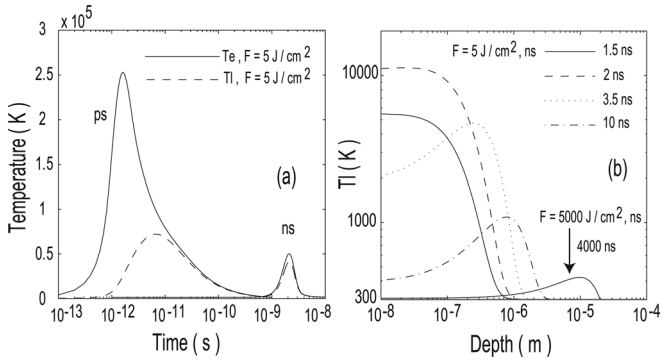

FIG. 1. (a) Time-dependence of electron T_e (solid line) and lattice T_l (dashed line) temperatures at the surface of a Sn target for FWHM = 1 ps and FWHM = 1 ns pulse durations and the same absorbed fluence of 5 J cm^{-2}. (b) The lattice temperature against a 40-μm-thick Sn target at different times for ns 5 J cm^{-2} and 5000 J cm^{-2} laser pulses. In the case of the 5000 J cm^{-2} laser pulse, the lattice temperature is shown at $t = 4000$ ns.

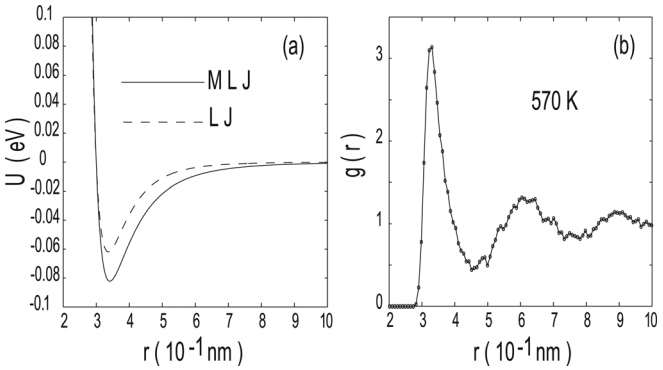

FIG. 2. (a) The modified Lennard-Jones (MLJ) pair-wise potential U_{MLJ} of liquid Sn (solid line) taken into account in the calculation. The original Lennard-Jones (LJ) potential (dashed line) with the same depth of the potential well ε is shown as a reference. (b) The calculated radial distribution function $g(r)$ of liquid Sn at 570 K.

temperatures at the surface of a Sn target immediately following Nd:YAG irradiation with 1.06 μm laser pulses of various durations with FWHM = 1 picosecond (ps) and 1 ns at the same absorbed fluence of 5 J cm^{-2}. Based on the classical approach of TTM, first, the electron subsystem is thermalized ($\simeq$fs) quickly due to laser energy absorptions; second, the lattice subsystem is warmed up ($\simeq$ps) through energy coupling with the electron subsystem. Figure 1(a) reveals that in the case of a ps pulse, the initial lattice heating due to the energy transfer from hot electrons takes about 10 ps and turns into cooling due to fast electron heat conduction to the bulk of the target at later times. The Sn target absorbs laser energy in a very thin region (skin-depth $\simeq$ 50 nm). Then, the thermal wave propagates into the bulk, followed by the shock wave. A comparison between the temperatures of ps and ns pulses shows that, as a result of the finite diffusivity and absorption coefficient, the thermal wave cannot penetrate deeply with a ps pulse. For a ns pulse, the time of the thermal wave propagation is sufficient that the Sn target can conduct heat away from the surface during the laser pulse. The lattice temperature against a 40-μm-thick Sn target at different times for ns 5 J cm^{-2} and 5000 J cm^{-2} laser pulses is shown in Fig. 1(b). In the case of the 5000 J cm^{-2} laser pulse, the lattice temperature is shown at $t = 4000$ ns. Please note that in the present article, for simplicity, we have not taken into account the effect of density variation due to the expansion of the target on the thermal conductivity, specific heat capacity, and absorption coefficient. Figure 1(b) shows that the lattice temperature inside the target ($\simeq 40$ μm) is much lower than that at its surface even at a very large fluence of 5000 J cm^{-2}. Within the framework of TTM, it follows from these calculations that during typical pre-pulse Nd:YAG 1.06 μm laser irradiation in EUV lithography experiments (ns pulse $I_0 \simeq 10^8$ to 10^{12} Wcm^{-2}), the Sn target rapidly reaches a high temperature. The large electron-phonon coupling constant and thermal conductivity of metals[31] can result in very high lattice heating and cooling rates of $\pm 10^{12}$ K/s or even more.

MD calculations are employed to study the thermodynamical pathway of bulk Sn at such high lattice heating and cooling rates and to verify the applicability of the aforementioned MLJ potential. The MLJ potential U_{MLJ} against the distance between two Sn atoms is shown in Fig. 2(a). In addition, Fig. 2(a) presents the original LJ potential with the same depth of the potential well as a reference. In the MLJ potential, the long-range attractive part of the LJ potential suitable for rare-gas liquids is modified to include the effect of the conduction electrons in liquid metals. Thus, the maximum depth in the MLJ potential is lower than that in the LJ potential with the same depth of the potential well as shown in Fig. 2(a). The calculated radial distribution function $g(r)$ of liquid Sn at 570 K and atmospheric pressure is shown in Fig. 2(b). The calculated $g(r)$ for liquid Sn using the MLJ potential, as compared with the result obtained via *ab initio* MD (Ref. 32) and the available experimental data presented in Ref. 33, is in good qualitative agreement. However, there are a few discrepancies, in particular in the height of the first maxima, although the positions remain almost unchanged. The calculations with either type of potential using *ab initio* values and MLJ at low temperature tend to overestimate the height of the first peak in $g(r)$ such that its obtained experimental value $\simeq 2.75$ at 573 K.

The MLJ potential is applied to study the caloric curve, melting temperature, rapid heating, and cooling processes via the MD method. Calculations were performed using two systems with 511 and 835 Sn atoms occupying ideal crystalline lattice positions under periodic boundary conditions. Due to the finite size of our system, a single equilibrium melting temperature cannot be found in a straightforward manner. According to hysteresis procedures,[23] we first decrease the temperature of the liquid Sn toward solidification and then raise the temperature of the solid in order to obtain the melting temperature. The simulated cell volumes V as a function of temperature in the cooling and heating cycles at atmospheric pressure, calculated using the system sizes of $N = 511$ and 835 Sn atoms, are shown in Fig. 3(a). We equilibrated the systems for 100 000 time steps (100 ps) using the NPT ensemble at $T = 900$ K. This was followed by a cooling process in which a system with a size of 835 (511) Sn atoms was cooled from 900 K to 300 K with a constant cooling rate ($\dot{T} = dT/dt$) of -0.3 Kps^{-1} (-0.5 Kps^{-1}). The sudden drop in volume at the solidification temperature (T_-)

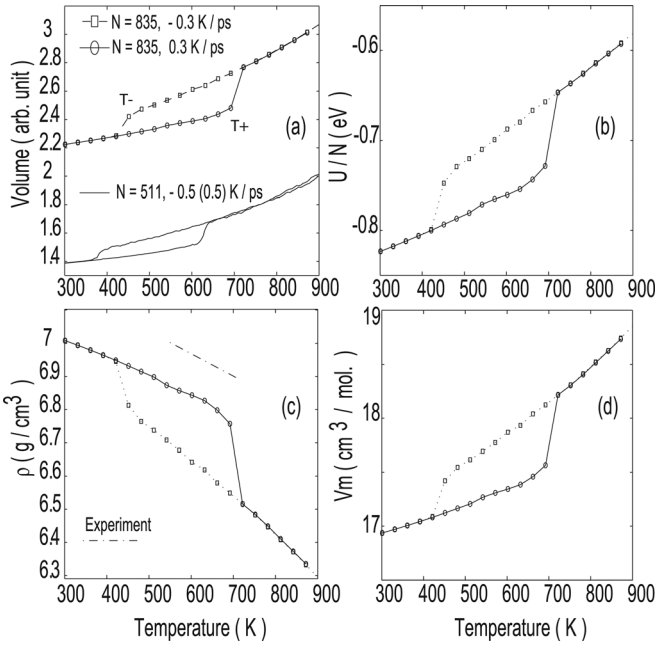

FIG. 3. The structural transitions of liquid Sn during a cooling-heating cycle based on the superheating-undercooling hysteresis method. (a) Simulated cell volumes upon cooling-heating cycles for two cases: the number of particles $N=835$ (511) and a cooling/heating rate of ± 0.3 (0.5) K/ps. (b) Potential energy per particle for the cooling-heating cycle. The variation of (c) the density and (d) the molar volume. These parameters are calculated using a system size of $N=835$ atoms.

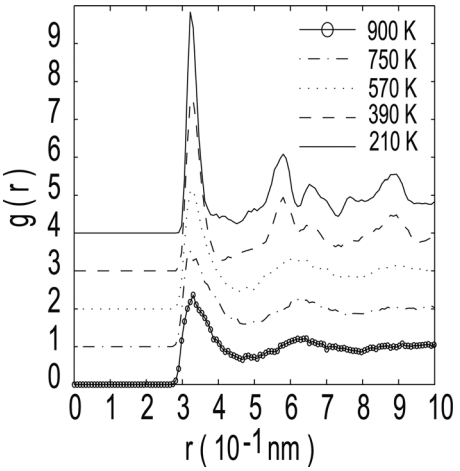

FIG. 4. The temperature dependence of the radial distribution function during the cooling phase as shown in Fig. 3. The curves are shifted for a better view. The cooling rate is -0.3 K/ps.

is shown in Fig. 3(a), demonstrating that the final system in the cooling phase is a crystalline state. The potential energy per atom (U/N, $N=835$), the density ρ, and the molar volume Vm. as a function of temperature upon cooling and heating are shown in Figs. 3(b), 3(c), and 3(d), respectively. In addition, the available experimental data for the density of liquid Sn (Ref. 34) in the temperature range of 505–775 K is shown in Fig. 3(c). The calculated results for the density and molar volume are in good agreement with the available data. The distinctive jump in the heating phase shown in Figs. 3(a), 3(b), 3(c), and 3(d), which starts after 600 K, indicates the phase transition from crystal to liquid Sn. The final state in the cooling phase can also be verified conveniently in terms of the results of the radial distribution function $g(r)$, as shown in Fig. 4. A characteristic liquid phase in the system with a size of 835 atoms appears in $g(r)$ as the temperature becomes higher than $\simeq 400$ K; in contrast, crystal peaks can be detected at temperatures lower than this and become more obvious with decreasing temperature. Please note that the evolution of $g(r)$ during the cooling process, as shown in Fig. 4, reveals that the MLJ potential or minimum of this potential results in a face centered cubic crystalline state at low temperature. However, the results of MD calculations, as shown in Figs. 3(c) and 3(d), are in good agreement with the available data for β-Sn crystal. In the hysteresis method, which is based on homogenous nucleation theory, the thermodynamic melting point (T_m) can be estimated as $T_m=T_+ + T_- - (T_+T_-)^{1/2}$, where T_+ and T_- are the maximum superheating and supercooling/undercooling temperatures, respectively. An inspection of Fig. 3(a) reveals that the superheating (supercooling) temperature T_+ (T_-) is $\simeq$690 (450) K for the system with 835 atoms and $\simeq 620$ (400) K in the case of 511 atoms, respectively. Thus, the T_m is $\simeq$ 580 (520) K in our calculation when using 835 (511) atoms. This is comparable to the experimental melting point of 505 K for pure Sn. Although the system including 511 atoms gives a T_m that is in better agreement with experimental data, it somewhat overestimates the density as compared to the experimental data due to the finite size effect. It is found that a system size larger than 835 atoms does not change results significantly.

The effect of cooling and heating rates on the thermodynamic pathway was qualitatively investigated using a system size of 511 Sn atoms. Figure 5(a) presents the volume of a simulated cell as a function of temperature at selected cooling rates and atmospheric pressures. The full hysteresis cycle upon cooling and heating processes is calculated using a constant rate of ± 0.5 K/ps as shown in Fig. 3(a). Two other lines are calculated at higher cooling rates of -5 and -10 K/ps. However, no crystallization could be observed in the temperature range of our calculation, indicating a very large hysteresis effect. This is surely related to the choice of cooling rate. Instead of crystallization, the system undergoes a glass transition from liquid to amorphous solid as the temperature is decreased.[35] It is well known that a first-order phase transition is characterized by not only stable phases, but also metastable phases. At a given temperature and pressure, the free energy of the metastable phase is greater than that of the stable phase. Superheated metastable states are formed when matter is subjected to a high heating rate. The effect of the heating rate on the melting point of a bulk Sn crystal is shown in Fig. 5(b). The volume as a function of temperature at atmospheric pressure is calculated for selected constant heating rates. The initial conditions for these trajectories correspond to one ensemble of the initial configurations at room temperature. The distinctive steps of the dependencies after a temperature of 600 K correspond to the transitions from metastable crystal to the liquid state. Superheated solid is a state of matter that can be realized experimentally only under particular conditions involving high rate energy impacts and/or very low concentrations of defects and impurities, which

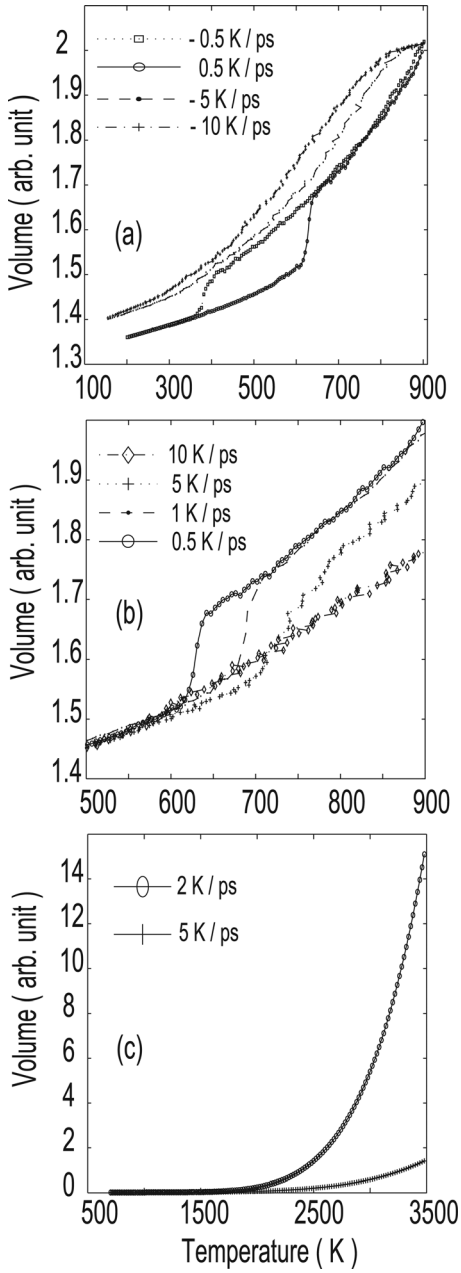

FIG. 5. (a) Liquid Sn is cooled down from 900 K at three selected cooling rates. The variation of the simulated cell volume with cooling rates of − 0.5, − 5, and − 10 K/ps is shown. In contrast to fast cooling rates, the slow cooling rate of − 0.5 K/ps and the same heating rate show the closed hysteresis cycle. (b) The dependence of the melting temperature of bulk Sn crystal on the heating rate. (c) The volume of a simulated cell containing liquid Sn as a function of the temperature at two constant heating rates. Please note that the abscissa scales are not the same.

enables heterogeneous melting. The simulations in Fig. 5(b) start from an initially ideal β-Sn crystal lattice without defects. A set of lifetime values of the superheated crystal structure at different temperatures can be obtained using a MD calculation. For example, the relaxation time is $\simeq$20 ps for Sn crystal heated up to 650 K with a heating rate of 1 K/ps. An inspection of the curves in Fig. 5(b) reveals that the melting temperature of the simulated perfect crystal system of Sn rises when the heating rate is elevated. As the heating rate increases, the system becomes highly randomized and might not have enough time to generate an equilibrium distribution, and thus the energy barrier for the phase transition decreases. In Fig. 5(c), the box volume is plotted as a function of the temperature when the liquid Sn is heated at two different heating rates. In the course of boiling, the simulation cell changes dramatically, which makes the box volume a suitable order parameter of the process in the NPT ensemble. The initial condition was liquid Sn at $\simeq$700 K. We equilibrated the systems for 100 000 time steps using an NPT ensemble at this temperature. This was followed by a heating process at atmospheric pressure in which a system of 511 Sn atoms was heated from 700 K to 3500 K with a constant heating rate. At a temperature of $\simeq$2500 K and a heating rate of 2 K/ps, the phase transition from a liquid to a gas state was observed by increasing the whole simulation system within a few hundreds of picoseconds. Please note that the thermodynamic boiling point of Sn is $\simeq$2700 K. An inspection of Fig. 5(c) reveals that when the heating rate rises, the thermal history changes the thermodynamic pathway, mainly owing to the inertial confinement effect. This means that superheated metastable liquid Sn is formed when it is subjected to a high heating rate. Under such heating conditions, the metal liquid phase can be superheated up to the maximum attainable superheating bounded by the spinodal temperature of $\simeq 0.8T_c$, where $T_c \simeq 5800$ K is the critical temperature.[28,36]

A mass limited Sn target is employed in single[6] or double laser pulse irradiation schemes[9,12] as a promising laser-based EUV source. It has been demonstrated that in single laser pulse experiments, a high CE is generated by Sn ions located within a 40 nm depth from the target surface. In the double pulse scheme, a Sn micro-droplet ($\simeq$40 μm in radius) has to be expanded before the main CO2 laser irradiation in order to improve the coupling efficiency between the long-wavelength CO2 laser and the target. For this purpose, pre-irradiation with a Nd:YAG laser prior to the main CO2 laser is indispensable. In this article, we are interested in estimating the maximum velocity of Sn particles against a typical fluence in EUV lithography experiments. Therefore, first, the temporal and spatial parameters of T_e and T_l are calculated using TTM for a ns (FWHM = 1 ns) Nd:YAG laser pulse at various intensities. The calculations were done for up to 4 μs. For decreasing calculation times, this time shrinks to 10 ps, and then the MD calculation coupled to a steady-state ionization model is used as a postprocessor in order to investigate the velocity distribution of a small Sn sample with a size of $\simeq 2 \times 2 \times 35$ nm. The cutoff radius for both potentials is assumed to be $\simeq 3\sigma$. In fact, this assumption underestimates the effect of the Coulomb potential in our calculation. The laser spot size is assumed to be much larger than the cross-section of our sample size. A schematic sketch of the calculation setup is shown in Fig. 6(a). First, we equilibrated the systems for 50 000 time steps (50 ps) using an NPT ensemble at $T \simeq 300$ K using the periodic boundary conditions. This was followed by 50 000 time steps using the NPT ensemble at the same temperature without a boundary condition in order to eliminate any stress in the system. Then, the laser irradiated in the z direction as shown in Fig. 6(a), and the computational conditions include the presence of no boundary condition (i.e., a small Sn sample in vacuum). The

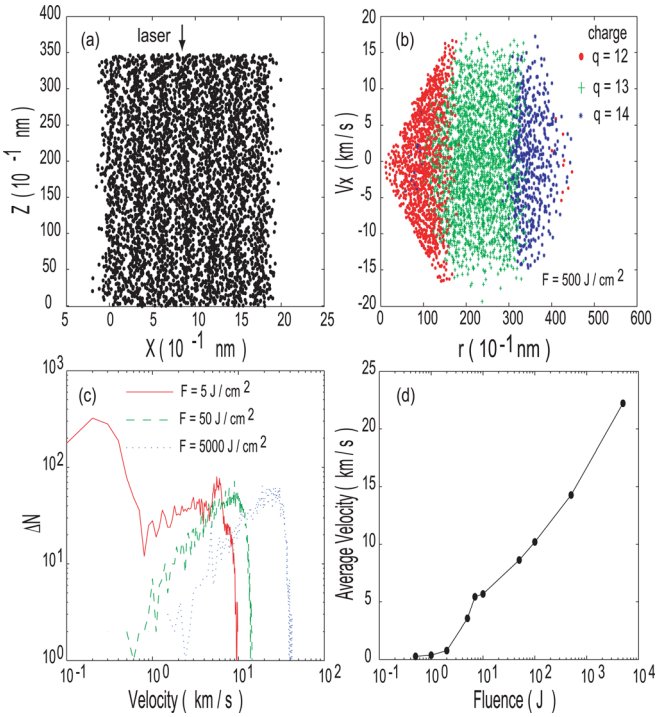

FIG. 6. (Color online) (a) The initial condition is assumed to be a small Sn sample size of $\simeq 2\times 2\times 35$ nm. A laser pulse is irradiated from the top surface of the sample. (b) A typical snapshot of particle velocities perpendicular to the laser direction and charge states against the norm of the position vector r before the maximum intensity of a laser pulse with a fluence of 500 J cm^{-2}. (c) The velocity distribution of Sn particles at various fluences of 5, 50, and 5000 J cm^{-2}. (d) The weighted average velocity values versus the laser fluence.

open boundary condition, meaning vacuum all around the sample, is appropriate to simulate a mass limited Sn target. Figure 6(b) presents a typical snapshot of ion velocities perpendicular to the laser direction and charge states against the norm of the position vector r before the maximum intensity of the laser pulse having a fluence of 500 J cm^{-2}. Figure 6(b) shows that under such conditions, the small sample almost fully disintegrates into individual highly ionized Sn atoms. Using the same calculation method, the velocity distribution of the particles is calculated at various fluences of 5, 50, and 5000 J cm^{-2}, as shown in Fig. 6(c). In the framework of our simple model, Fig. 6(c) reveals that ejected Sn ions have a maximum velocity on the order of $\simeq$10 to 40 km/s in plasma created using a ns Nd:YAG laser with a fluence in the range of 5–5000 J cm^{-2}. The results are in good agreement with experimental data as discussed in Refs. 4 and 13. The weighted average velocity values versus the laser fluence are shown in Fig. 6(d). The increase in the laser fluence leads to the higher expansion velocities of the ejected ions as shown in Fig. 6(d). However, the increase of the velocity is not monotonic at low laser fluence. A sudden jump of the velocity is seen at a laser fluence of $\simeq$ 2 J cm^{-2}. The maximum lattice temperature at this fluence is $\simeq$3000 to 3500 K. This fluence is almost the ablation (boiling) threshold F_b of Sn in the case of a ns laser pulse. At a fluence less than F_b, melting and spallation occur.[37] Our calculation shows that a fluence of $\simeq$ 5 J cm^{-2} is the plasma (ionization) threshold. Please note that the sample size in our calculation is a very small fraction of a Sn target ($\simeq$ 40 μm) in the present double laser pulse irradiation scheme. In the case of high fluence ($\gtrsim$10 J cm^{-2}) in our calculation, the initial temperature in our sample or in the vicinity of the actual Sn target surface in experiments [depth $\lesssim 1/\alpha \lesssim$ 50 nm, or even larger, as shown in Fig. 1(b)] is high enough that direct atomization occurs, so that the phase trajectories from this layer go above the critical point of Sn and the target is directly transformed into the gas or plasma phase. However, based on the energy deposition, different mechanisms exist in the rest of the target. The calculation using the TTM as shown in Fig. 1(b) shows that for an extremely high fluence of 5000 J cm^{-2}, the temperature in the rear of the target (deeper than 10 μm) is very low ($\simeq$400 K) even after 4 μs. This temperature corresponds to the surface temperature when irradiated by a ns laser having a fluence of $\lesssim$0.1 J cm^{-2}. This part of the target is a source of neutral debris in a single pulse laser scheme. Such investigation is in progress in our laboratory, but the details are beyond the scope of the present study.

IV. CONCLUSIONS

Using the classical approach of a two-temperature model, it is found that the large electron-phonon coupling constant and thermal conductivity of a tin target irradiated by a ns Nd:YAG (1.06 μm) laser in a typical extreme ultraviolet lithography experiment can result in very high lattice heating and cooling rates of $\pm 10^{12}$ K/s or even more. Using molecular dynamics calculations based on a simple modified Lennard-Jones potential, the caloric curves of the solid and liquid phases and the melting and boiling temperatures are investigated. The potential gives reasonable results, for instance, for both density and molar volume in a wide range of temperatures. The calculated radial distribution functions for liquid tin near the melting point are comparable to the experimental data. The calculation results at selected high cooling and heating rates have shown superheating and supercooling effects on the thermodynamic pathways. It was found that with a fast heating rate, the melting and boiling temperatures of a bulk tin sample show a kinetic process that is largely affected by the thermal history. The velocity distribution of tin particles versus the fluence is investigated using a simplified method including a one-dimensional two-temperature molecular dynamics based on the modified Lennard-Jones and Coulomb potentials, and a steady-state ionization model. The ablation and plasma (ionization) thresholds of tin are estimated to be $\simeq$ 2 and 5 J cm^{-2} in the case of a ns laser pulse. In the framework of our model, it was found that ejected Sn particles have a maximum velocity on the order of 10 to 40 km/s in plasma created using a ns Nd:YAG laser having a fluence in the range of 5-5000 J cm^{-2}.

ACKNOWLEDGMENTS

This work was sponsored in part by the New Energy and Industrial Technology Development Organization (NEDO) and the Extreme Ultraviolet Lithography System Development Association (EUVA) of Japan.

[1]See several contributions presented at the 2008 International Symposium on Extreme Ultraviolet Lithography, Lake Tahoe, CA, 28 September 2008.
[2]N. R. Bwering, I. V. Fomenkov, D. C. Brandt, A. N. Bykanov, A. I. Ershov, W. N. Partlo, D. W. Myers, N. R. Farrar, G. O. Vaschenko, O. V. Khodykin, J. R. Hoffman, C. P. Chrobak, S. N. Srivastava, I. A. Chirag, R. Daniel, G. David, A. Vidusek, S. De Dea Richard, and R. Hou, J. Micro/Nanolith. MEMS MOEMS **8**, 041504 (2009).
[3]M. W. McGeoch, J. Phys. D **43**, 105201 (2010).
[4]R. W. Coons, S. S. Harilal, D. Campos, and A. Hassanein, J. Appl. Phys. **108**, 063306 (2010).
[5]D. Campos, S. S. Harilal, and A. Hassanein, J. Appl. Phys. **108**, 113305 (2010).
[6]M. Shimomura, S. Fujioka, T. Ando, H. Sakaguchi, Y. Nakai, Y. Yasuda, H. Nishimura, K. Nagai, T. Norimatsu, K. Nishihara, N. Miyanaga, Y. Izawa, and K. Mima, Appl. Phys. Express **1**, 056001 (2008).
[7]S. S. Harilal, T. Sizyuk, and A. Hassanein, Appl. Phys. Lett. **96**, 111503 (2010).
[8]M. Masnavi, M. Nakajima, E. Hotta, K. Horioka, G. Niimi, and A. Sasaki, J. Appl. Phys. **101**, 033306 (2007).
[9]J. R. Hoffman, A. N. Bykanov, O. V. Khodykin, A. I. Ershov, N. R. Bowering, I. V. Fomenkov, W. N. Partlo, and D. W. Myers, Proc. SPIE **5751**, 892 (2005).
[10]Y. Tao, M. S. Tillack, K. L. Sequoia, and F. Najimabadi, Proc. SPIE **6517**, 65173Q (2007).
[11]K. Nishihara, A. Sunahara, A. Sasaki, M. Nunami, H. Tanuma, S. Fujioka, Y. Shimada, K. Fujima, H. Furukawa, T. Kato, F. Koike, R. More, M. Murakami, T. Nishikawa, V. Zhakhovskii, K. Gamata, A. Takata, H. Ueda, H. Nishimura, Y. Izawa, N. Miyanaga, and K. Mima, Phys. Plasmas **15**, 056708 (2008).
[12]H. Mizoguchi, T. Abe, Y. Watanabe, T. Ishihara, T. Ohta, T. Hori, A. Kurosu, H. Komori, K. Kakizaki, A. Sumitani, O. Wakabayashi, H. Nakarai, J. Fujimoto, and A. Endo, Proc. SPIE **7636**, 763608 (2010).
[13]T. Akiyama, K. Okazaki, D. Nakamura, A. Takahashi, and T. Okada, J. Plasma Fusion Res. **8**, 496 (2009).
[14]S. I. Anisimov and B. Rethfeld, Proc. SPIE **3093**, 192 (1997).
[15]T. W. Chapman, Mater. Sci. Eng. **1**, 65 (1966).
[16]E. Kannatey-Asibu, *Principles of Laser Materials Processing* (John Wiley & Sons, New York, 2009).
[17]Z. Lin, L. V. Zhigilei, and V. Celli, Phys. Rev. B **77**, 075133 (2008).
[18]J. D. Kress, L. A. Collins, S. Mazevet, and D. A. Horner, AIP Conf. Proc. **955**, 1433 (2008).
[19]R. E. Lindquist and A. W. Ewald, Phys. Rev. **135**, A191 (1964).
[20]M. Griebel, S. Knapek, and G. Zumbusch, *Numerical Simulation in Molecular Dynamics: Numerics, Algorithms, Parallelization, Applications* (Springer, New York, 2007).
[21]Y. N. Zhang, L. Wang, S. Morioka, and W. M. Wang, Phys. Rev. B **57**, 014106 (2007).
[22]S. Morioka, J. Non-Cryst. Solids **341**, 46 (2004).
[23]S. N. Luo, T. J. Ahrens, T. Cagin, A. Strachen, W. A. Goddard, and D. C. Swift, Phys. Rev. B **68**, 134206 (2003).
[24]X. Liu, C. Meng, and C. Liu, Phase Trans. **79**, 249 (2006).
[25]G. E. Norman and V. V. Stegailov, Mol. Simul. **30**, 397 (2004).
[26]B. J. Garrison, T. E. Itina, and L. V. Zhigilei, Phys. Rev. E **68**, 041501 (2003).
[27]H. J. C. Berendsen, J. P. M. Postma, W. F. Van Gunsteren, A. DiNola, and J. R. Haak, J. Chem. Phys. **81**, 3684 (1984).
[28]C. Cheng and X. Xu, Phys. Rev. B **72**, 165415 (2005).
[29]X. Wang and X. Xu, J. Heat Trans. **125**, 1147 (2003).
[30]X. Wang, J. Phys. D **38**, 1805 (2005).
[31]W. H. Duff and L. V. Zhigilei, J. Phys.: Conf. Ser. **59**, 413 (2007).
[32]L. Calderin, D. J. Gonzalez, L. E. Gonzalez, and J. M. Lopez, J. Chem. Phys. **129**, 194506 (2008).
[33]T. Itami, S. Munejiri, T. Masaki, H. Aoki, Y. Ishii, T. Kamiyama, Y. Senda, F. Shimojo, and K. Hoshino, Phys. Rev. B **67**, 064201 (2003).
[34]S. B. Alchagirov and A. M. Chochaeva, High Temp. **38**, 44 (2000).
[35]Y. Qi, T. Cagin, Y. Kimura, and W. A. Goddard, Phys. Rev. B **59**, 3527 (1999).
[36]R. Balasubramanian, Int. J. Thermophys. **27**, 1494 (2006).
[37]L. V. Zhigilei, Z. Lin, and D. S. Ivanov, J. Phys. Chem. C **113**, 11892 (2009).